Glancing angle deposited CdTe: Nanostructured films and impact on solar cell performance

Dipendra Adhikari, Maxwell M. Junda, Ebin Bastola, Prakash Koirala, Randall J. Ellingson, Robert W. Collins, Nikolas J. Podraza[*]

Wright Center for Photovoltaics Innovation and Commercialization & Department of Physics and Astronomy, University of Toledo, Toledo, OH, 43606, USA

ARTICLE INFO

ABSTRACT

Cadmium telluride (CdTe) thin films with different microstructures and optical properties have been produced on soda-lime glass by glancing angle deposition (GLAD) at oblique sputtering angles varying from 0° to 80° with respect to the substrate normal. From cross-sectional scanning electron micrographs, increasingly tilted columnar structure occurs with increasing incident angle for as-deposited CdTe films. CdTe films deposited at lower angles closer to normal incidence consist of a mixture of cubic zinc blende and hexagonal wurtzite crystal structures while films prepared at more oblique angles have hexagonal wurtzite crystal structure. Post-deposition CdCl$_2$ treated films show enhancement in crystallite/grain size for samples prepared under all conditions. The optical response in the form of the complex dielectric function ($\varepsilon = \varepsilon_1 + i\varepsilon_2$) spectra from 0.74 to 5.89 eV for the GLAD thin films are all qualitatively similar to single crystal CdTe. Higher angle deposited samples show columnar structure induced anisotropy in spectra in ε in the transparent spectral range. Application of GLAD CdTe interlayers between CdS and CdTe of the standard CdS/CdTe heterojunction design solar cell shows better performance with up to 0.9% absolute efficiency increase.

1. Introduction

Cadmium telluride (CdTe) is a II-VI compound semiconductor with high optical absorption $> 10^4 \, \mathrm{cm}^{-1}$ in the visible spectral range and a direct band gap ~1.5 eV, making it an ideal absorber layer material in thin film photovoltaics (PV). CdTe is a stable material under outdoor conditions and can be deposited using various methods including sputtering [1–5], spray pyrolysis [6], electrodeposition [7], and close-space sublimation [8,9]. Recently, the champion PV device efficiencies reached 22.1% for a thin film CdTe research solar cell and 18.6% for a module, respectively [10]. The best efficiencies of solar cells incorporating sputtered CdTe absorbers are about 14% [1,11]. Current research in the field is focused on making highly efficient devices by alternative deposition techniques for better quality CdTe absorbers, improving back contact performance and compatibility, and modification of *p/n* interfaces [12] to enhance photogenerated carrier collection.

The microstructure of CdTe films depends on deposition conditions and plays an important role in PV device performance, which depends upon the characteristics of both crystalline grains and surrounding grain boundary material. Previous reports indicate that depleted grain boundaries are beneficial to CdTe solar cell performance by helping to

separate carriers, suppress recombination, and improve carrier collection [4,13,14]. A CdS window layer is a commonly used *n*-type heterojunction partner with a *p*-type CdTe absorber. Cubic zinc blende CdTe is thermodynamically stable at room temperature, but exhibits a high lattice mismatch with room temperature stable hexagonal wurtzite CdS [15]. However, hexagonal wurtzite and mixed phase zinc blende + wurtzite CdTe films have been deposited at low temperature by vacuum evaporation and sputtering [15–17].

Glancing angle deposition (GLAD) produces films with varying preferential grain orientations and grain boundary configurations [18]. GLAD involves separating the source flux and substrate target normals by an oblique angle. The dependence of crystal structure, grain size, grain orientation, and optical properties on oblique sputtering angle are identified. Previous works [17,18] show that opto-electronic and microstructural properties of the deposited film can be effectively manipulated using GLAD. The microstructure of CdTe films can potentially be engineered, resulting in the ability to tune opto-electronic properties for PV device optimization, such as by tailoring material structure at the *p/n* interface. This work involves study of such CdTe films deposited via radio frequency (RF) magnetron sputtering with material flux at a range of angles relative to the substrate normal and evaluation of PV device

performance by incorporating GLAD CdTe. In particular, the influence of deposition angle on the microstructural and optical properties of sputtered CdTe film are studied and improvement of PV device performance by incorporating a 100 nm GLAD interlayer at the *p/n* junction is demonstrated. The crystal structure and the crystallite size are obtained from x-ray diffraction (XRD), cross-section and surface microstructures are imaged from scanning electron microscopy (SEM), and complex optical properties are extracted from spectroscopic ellipsometry. The oblique angle of deposition manipulates crystal structure, grain size, grain orientation, and optical properties. The effect of CdCl$_2$ post-deposition processing on crystallite size enhancement as a function of treatment time on GLAD CdTe is tracked. A nominally 100 nm thick structurally engineered GLAD CdTe interlayer is introduced between the *n*-type CdS window layer and *p*-type CdTe absorber in solar cells. Power conversion efficiency (*PCE*), open circuit voltage (*V$_{OC}$*), and fill factor (*FF*) improve with introduction of this GLAD CdTe interlayer between CdS and CdTe layers of a conventional CdS/CdTe heterojunction solar cell.

2. Experimental methods

RF magnetron sputtered (frequency = 13.56 MHz) CdTe films have been deposited at room temperature (RT) onto soda-lime glass substrates using GLAD in a standalone vacuum chamber (AXXIS™, K. J. Lesker Co.). The glass substrates are cleaned ultrasonically, rinsed with deionized water, and blown dry with nitrogen before film deposition. A schematic diagram of the GLAD process is shown in the Fig. 1. Films are deposited at angles (Φ) of 0°, 20°, 40°, 60°, and 80° as defined by the angle between the normal extending from the center of the sputtering target and the normal extending from the center of the substrate.

A 7.62 cm diameter 99.999% purity CdTe target is sputtered for 70 min in a 15 mTorr pressure Ar ambient at 100 W RF target power. The distance from the center of the target to the center of the substrate is 13.4 cm. The substrate remains stationary during deposition. The deposition rate of material in the center of the substrate is 28.1 nm/min at Φ = 0° and slightly decreases with increasing angle Φ to 22.1 nm/min at Φ = 80°. Post-deposition CdCl$_2$ heat treatment is performed by wetting the film surface with a saturated solution of CdCl$_2$ in methanol followed by heating at 387 °C in dry air ambient for 10, 20, 30, or 40 min [3–5]. The CdCl$_2$ process is standard for CdTe PV as it increases CdTe grain/crystallite size and results in higher *PCE* devices. Cross-sectional and surface images are obtained from SEM (Hitachi S-4800). XRD patterns (Rigaku Ultima III diffractometer) are analyzed to obtain the crystal structure and crystallite size. A silicon sample is used for calibration of the diffractometer. *Ex-situ* spectroscopic ellipsometric and Mueller matrix spectra have been collected by using single rotating compensator (M-2000FI, J. A. Woollam Co. Inc.) [19,20] and dual
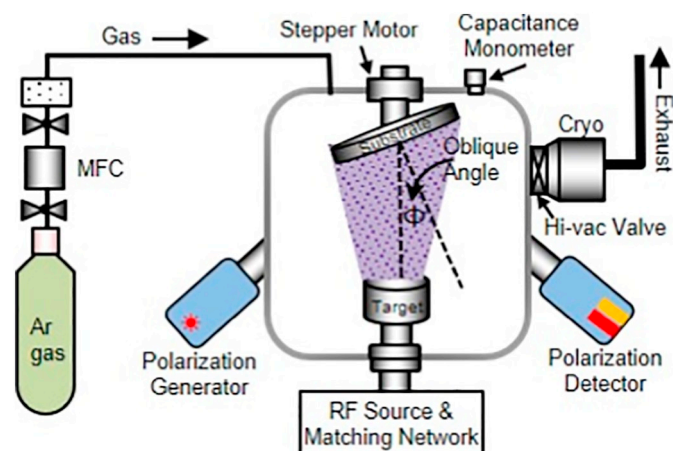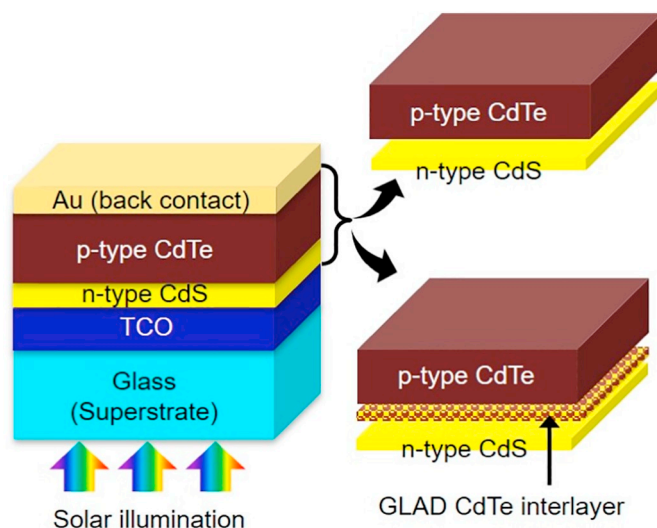
Fig. 2. Schematic diagram of CdS/CdTe heterojunction solar cells with and without a thin GLAD CdTe interlayer between the wurtzite CdS and zinc blende CdTe layers.

rotating compensator [21] (RC2, J. A. Woollam Co. Inc.) multichannel ellipsometers. Optical spectra are collected from near the center of each sample. Complex optical response and optical anisotropy resulting from columnar structure are obtained from analysis of ellipsometric and Mueller matrix spectra collected for GLAD CdTe films.

CdS/CdTe heterojunction solar cells are fabricated in the superstrate configuration, as shown in the schematic diagrams in Fig. 2. Solar cells are fabricated with and without a GLAD CdTe interlayer prepared at Φ = 80°, which exhibits wurtzite crystal structure. The superstrates are 15.24 cm X 15.24 cm soda lime glass coated by 300–400 nm of SnO$_2$:F with an additional 100 nm of high resistivity transparent SnO$_2$ to form the transparent conducting oxide (TCO) front contact to the device (TEC-15 M, Pilkington North America). The solar cell fabrication sequence begins with magnetron sputter deposition of 100 nm *n*-type CdS followed by a 2 μm *p*-type CdTe absorber. These layers are then subjected to the aforementioned CdCl$_2$ heat treatment for 30 min. The solar cell is completed by RT thermal evaporation of 3 nm Cu and 40 nm Au through a dot shadow mask to form the back electrical contact. The completed cell structure is annealed at 150 °C in air for 30 min to promote Cu diffusion into CdTe. Cu does not exist as a discrete layer in the final devices as it fully diffuses into CdTe, lightly doping it. 256 individual dot solar cells each having an active area of 0.126 cm^2 are formed for each process. The deposition parameters used during the fabrication of each component layer of the complete solar cells are listed in Table 1.

Photocurrent density versus voltage (*J-V*) are measured under simulated one sun AM1.5G (100 mW/cm^2) illumination from a 450 W

Fig. 1. Schematic of glancing angle deposition (GLAD) sputtering.

Table 1
Deposition conditions for the individual solar cell layers. "RT" denotes room temperature.

Layer type	Deposition method	Deposition parameters			
		Substrate temperature (°C)	Target power (W)	Pressure (mTorr)	Ar gas flow (SCCM)
CdS	RF sputter	250	200	15	23
CdTe interlayer	Φ = 80° GLAD	RT	100	15	23
CdTe	RF sputter	RT	100	15	23
Cu	Evaporation	RT	–	10^{-3}	–
Au	Evaporation	RT	–	10^{-3}	–
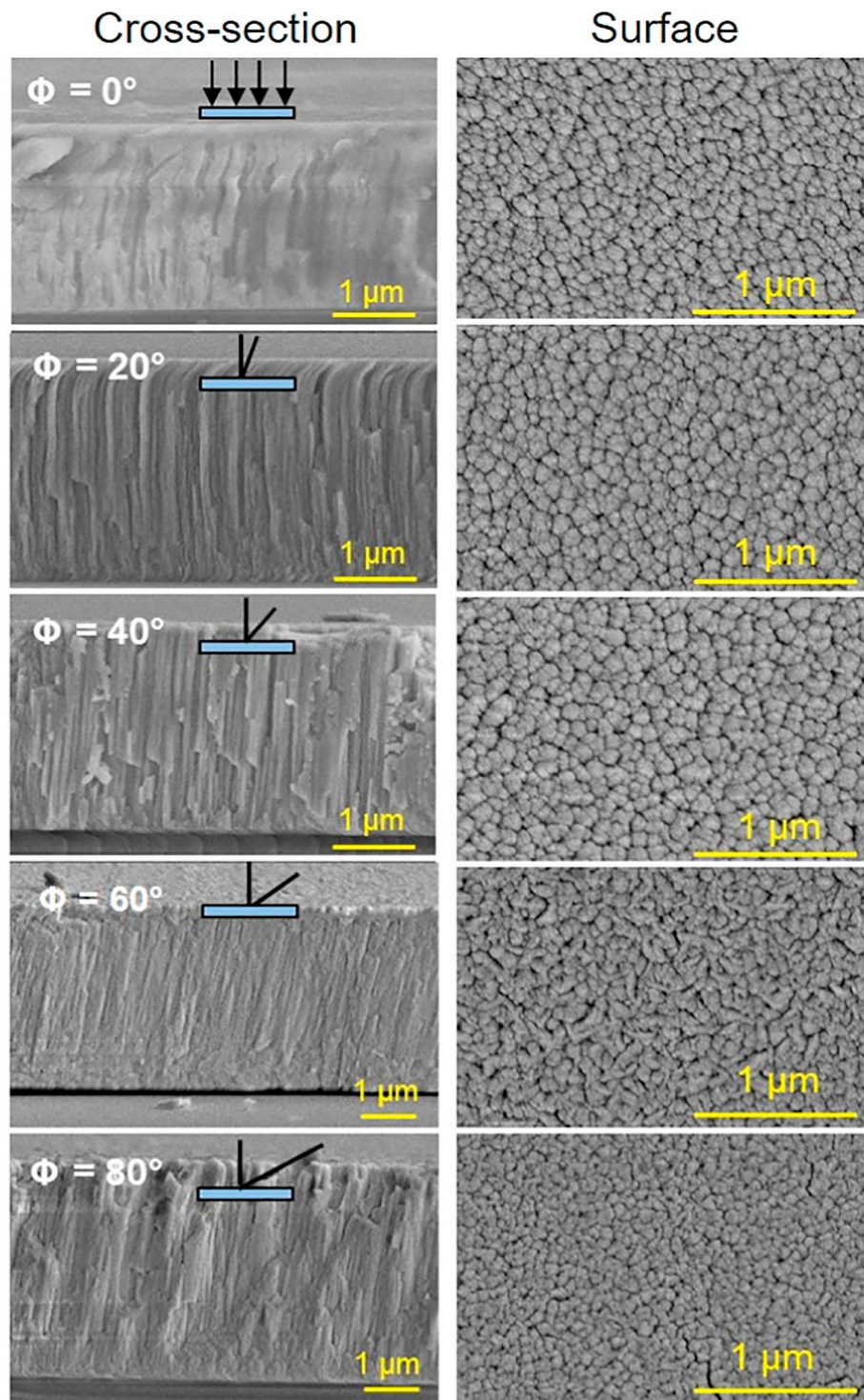
Fig. 3. Cross-sectional and surface scanning electron micrographs (SEMs) of as-deposited GLAD CdTe films prepared as functions of oblique angles with respect to the substrate normal.

Xenon light source (Oriel, Model 9119, Newport) with a digital source meter (Keithley 2440) in air at room temperature. External quantum efficiency (EQE) measurements are performed (model IVQE8-C, PV Instruments) to characterize spectrally resolved device performance.

3. Results and discussion

Fig. 3 shows cross-sectional and surface SEM of as-deposited CdTe prepared at different oblique angles. The cross-sections show that the films have slanted columnar structure inclined towards the incoming material flux during sputtering. The angle of column inclination relative to substrate normal is much smaller than the incident oblique angle but increases with increasing angles [17]. This behavior is expected as atomic scale self-shadowing effects are more pronounced at more oblique deposition angles, resulting in continued growth of initial nuclei on the substrate as lengthening columns due to low diffusion lengths of precursors on the surface [17,22,23]. In general, columnar GLAD films have lower columnar tilt angle than oblique deposition angle with even
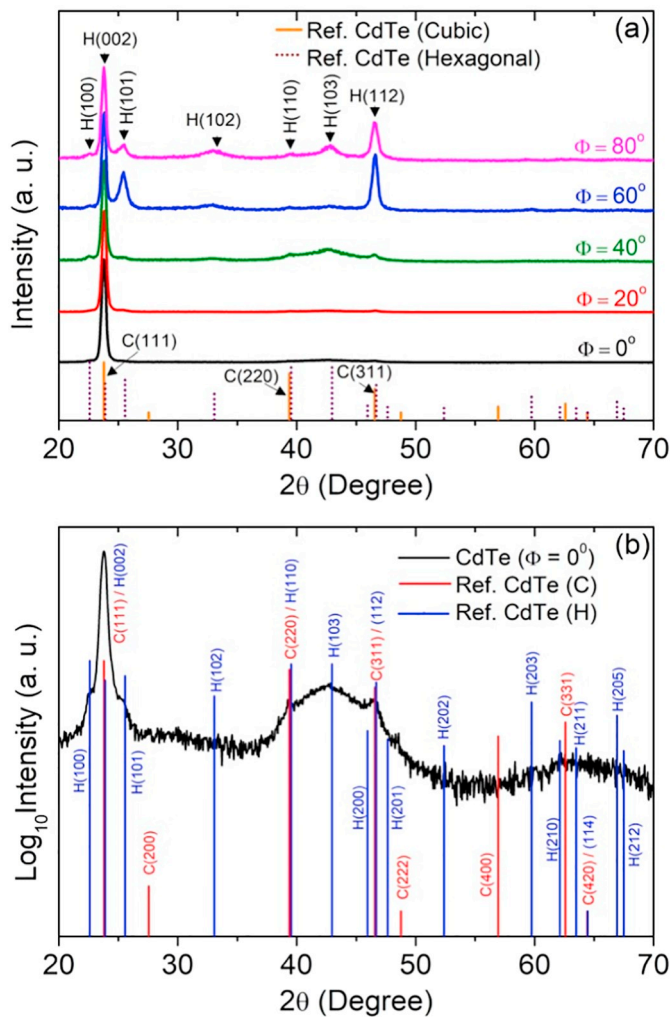
Fig. 4. X-ray diffraction (XRD) patterns of (a) as-deposited CdTe sputtered on soda-lime glass at different oblique angles (Φ) and (b) Log scale XRD of as-deposited CdTe sputtered at Φ = 0°. The reference lines are for standard cubic zinc blende CdTe [PDF # 97-010-8238] and hexagonal wurtzite CdTe [PDF # 97-015-0941] obtained from MDI JADE software.

further reduction in tilt angle when scattering in the gas phase becomes more substantial [24–31]. The surface microstructure of the films vary as the oblique angle is increased. The surface morphology of the films

deposited at Φ = 60° and 80° appear substantially different from other films deposited at lower Φ, which may be due to higher columnar tilt angle, crystal phase transitions from mixed (cubic + hexagonal) to hexagonal at higher Φ, or both. The relatively low substrate temperature is expected to result in low diffusion lengths of precursors on the growing surface, enabling the formation of the metastable wurtzite phase instead of the stable zinc blende phase. At low angles the films are mixed phase. At higher oblique angles the low diffusion length of precursors coupled with enhanced atomic scale self-shadowing results in the metastable wurtzite phase formation. Surface view SEM of as-deposited films in Fig. 3 shows variation in grain size from 126 ± 7 to 87 ± 5 nm among the films with the Φ = 80° sample consisting of the smallest grains.

XRD patterns for the as-deposited CdTe films are shown in Fig. 4. The samples deposited with small oblique angles Φ < 40° show the highest intensity XRD peak at 2θ ~23.7° which is ascribed to both cubic (C) zinc blende and hexagonal (H) wurtzite phases with C(111) and H (002) Miller index planes, respectively. Although literature reports that cubic CdTe is produced when sputtered normal to substrate (lower angle Φ) and at lower temperature close to room temperature (RT) [32–34], low intensity but distinct C(222), H(100), H(101), and H(103) peaks are observed here in as-deposited GLAD CdTe films at Φ < 40° as shown for Φ = 0° in the Fig. 4(b). Films deposited at Φ < 40° are considered to be mixed phase cubic and hexagonal CdTe. As the oblique angle is increased Φ ≥ 40°, diffraction peaks associated with only the cubic phase are not observed. Crystallite size obtained from the XRD analysis for the same samples is lower compared to grain size obtained from SEM indicating that these grains are composed of multiple crystallites, the mean free path of electrons is limited by defects and smaller than the grain, or both.

Isotropic optical response in the form of the complex dielectric function ($\varepsilon = \varepsilon_1 + i\varepsilon_2$) spectra of all as-deposited GLAD CdTe films are obtained by fitting parametric optical and layer structural models to measured ellipsometric spectra from 0.74–5.89 eV using a least squares regression that minimizes the unweighted error function [35] between measured and model-simulated ellipsometric spectra. Structurally, the models consist of a semi-infinite glass substrate, bulk CdTe layer thickness d_b, and surface roughness thickness d_s as shown schematically in Fig. 5. The optical properties of bulk CdTe are initially parameterized by a sum of critical point oscillators assuming parabolic bands (CPPB) [36,37] and a Tauc-Lorentz oscillator [38,39] to describe electronic band-to-band transitions. The optical response of the surface roughness is described by multiple Bruggeman effective medium approximation (EMA) [40] layers consisting of f_v volume fraction void and $1 - f_v$ fraction material identical to the underlying bulk CdTe. Three effective medium layers are needed to describe the complicated surface
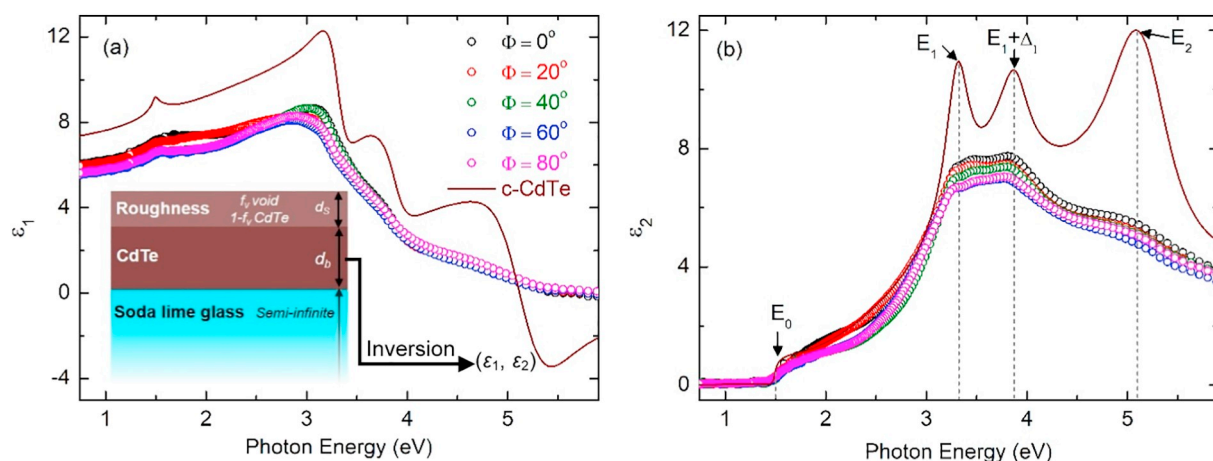
Fig. 5. Complex dielectric function ($\varepsilon = \varepsilon_1 + i\varepsilon_2$) spectra of as-deposited GLAD polycrystalline CdTe films produced at different oblique angles during sputtering. The optical response of single crystal (c-CdTe) is included for comparison [45], and the structural model schematic is shown in the inset.

Table 2
Structural parameters including surface roughness thickness (d_s), void fraction percentage in each effective medium approximation (EMA) layer comprising the surface roughness layer (f_v), and bulk film thickness (d_b) for as-deposited CdTe at different oblique angles (Φ) between the substrate normal and target normal.

Φ	Bulk thick. (nm)	Surface roughness thicknesses (d_s) and void fractions (f_v)						Eff. thick. (nm)
		EMA1		EMA2		EMA3		
		Thickness (nm)	Void fraction (%)	Thickness (nm)	Void fraction (%)	Thickness (nm)	Void fraction (%)	
0°	1758 ± 9	151 ± 10	1.7 ± 0.3	49 ± 7	7 ± 2	28 ± 3	39 ± 2	1968 ± 27
20°	1716 ± 8	148 ± 15	1.2 ± 0.2	32 ± 10	6 ± 4	25 ± 4	37 ± 3	1908 ± 37
40°	1544 ± 15	175 ± 30	0.6 ± 0.3	40 ± 24	4 ± 3	29 ± 5	39 ± 3	1775 ± 72
60°	1318 ± 7	160 ± 11	1.0 ± 0.2	49 ± 8	4 ± 1	32 ± 2	35 ± 1	1545 ± 26
80°	1307 ± 7	166 ± 12	0.8 ± 0.2	53 ± 9	3 ± 1	31 ± 1	32 ± 1	1544 ± 29

roughness of combined thickness d_s, f_v of each layer is allowed to vary independently resulting in monotonically increasing f_v towards the outermost EMA layer and the ambient interface. This three EMA layer model is found to be necessary to accurately describe the relatively rough surface where there is a gradient in f_v. This multiple layer approach to describe surface roughness with depth is necessary as sputtered CdTe and CdS morphology with depth can become quite complicated even for normal incidence sputtered films [41–43]. All the structural parameters including d_s, f_v, d_b, and effective film thickness for as-deposited CdTe at different Φ are reported in Table 2. The thickness and the relative void fraction in each EMA layer representing surface roughness are similar for all films, with the difference in effective film thickness primarily from the bulk film thickness. Effective film thickness is defined as the sum of d_b plus each EMA layer thickness weighted by $1-f_v$ and monotonically from 1968 ± 27 nm for $\Phi = 0°$ to 1544 ± 29 nm for $\Phi = 80°$. All the films were deposited for 70 min, and this variation in effective film thickness with Φ is expected for GLAD films. After initially using a parametric ε to determine structural parameters, ε describing the bulk CdTe is obtained by numerical inversion [44] in Fig. 5. For all films, ε_1 at low photon energies in the transparent spectral range are substantially lower compared to single crystal CdTe (c-CdTe). A Bruggeman EMA consisting of fractions of void and c-CdTe is fit to ε_1 at 0.74 eV obtained for all films as a proxy for relative density of the films. These films become less dense with increasing Φ with $1-f_v$ decreasing from 0.86 for $\Phi = 0°$ to 0.80 for $\Phi = 80°$. The observed columnar tilt angles and the relative density of the films in this study seems small compared to the range in Φ. Low substrate temperature results in low surface precursor diffusion lengths, and the process pressure results in high gas scattering. The relatively small columnar tilt angles are expected based on these process conditions and consistent with similar films in literature [28–31]. The decreasing density resulting from higher oblique angles is due to increased columnar self-shadowing [17], transition in crystal structure, or both. By fitting CPPB oscillators directly to the first derivative of numerically inverted ε_2 ($d\varepsilon_2/dE$) with respect to photon energy, four critical point features describing the E_0, E_1, $E_1+\Delta_1$, and E_2 electronic transitions are determined to have resonance energies ranging from 1.49 ± 0.20 to 1.54 ± 0.20 eV, 3.24 ± 0.30 to 3.27 ± 0.30, 3.37 ± 0.06 to 4.00 ± 0.20 eV, and 4.20 ± 0.11 to 4.77 ± 0.30 eV, respectively. These values are close to those known for c-CdTe at 1.491, 3.310, 3.894, and 5.160 eV [45–47]. Sensitivity to the $E_1+\Delta_1$ and E_2 critical point energies may be lost in the films due to the complicated surface roughness structure, small grain/crystallite size, low critical point amplitude, and wide critical point broadening. Zinc blende cubic CdTe exhibits lower band gap energy compared to wurtzite hexagonal CdTe [48,49]. Here, the band gap energy (E_g) of all as-deposited CdTe as a function of Φ are obtained from spectroscopic ellipsometry. Lower band gap values E_g ~1.50 eV are observed for $\Phi < 40°$ and higher values E_g ~1.53 eV for $\Phi \geq 40°$. Although these band gap values are close and may be impacted by film stress as well, the behavior corresponds to structural trends from XRD. All these observations indicate

that the wurtzite hexagonal phase is favored at higher values of Φ.

The columnar structures of these films are substantially inclined away from substrate normal, about 12° in the cross-sectional SEMs for films deposited at $\Phi = 60°$ and 80°. In-plane optical anisotropy would be expected for the films deposited at high Φ because of the projection of sampling of the polar Euler angle rotated columns, $\theta = 12°$ in this case. Mueller matrix spectra are measured at three azimuthal angles ($\varphi = 0$, 45, and 90°) of rotation about the substrate normal and simultaneous modeling of all three sets of spectra is performed using a similar procedure to that explained in Ref. [50]. Mueller matrix elements normalized to M_{11} sensitive to sample rotations (m_{13}, m_{14}, m_{23}, m_{24}, m_{31}, m_{32}, m_{41}, m_{42}) in the transparent spectral range are fit. The 0.74–1.23 eV photon energy range is chosen to simplify the optical property model by avoiding substantial absorption above the band gap due to electronic transitions and the highest contribution to absorption below the band gap due to Urbach tails. To describe optical anisotropy in the films deposited at $\Phi = 60°$ and 80°, a uniaxial model is employed. The parametric optical response for both of these films is obtained by fitting a Sellmeier expression [37] to describe the ε_1 spectra shown in Fig. 5 over the 0.74–1.23 eV transparent wavelength range. These spectra are then input into EMAs alongside a variable fraction void to describe both optical properties parallel (extra-ordinary) and perpendicular (ordinary) to the columnar principal axes. For each film, the void fraction in both ordinary and extraordinary directions are held common. Limiting forms of effective medium theory are employed [51] in which the ordinary direction exhibits maximum electric field screening (screening parameter = 1) and the extraordinary direction exhibits minimum electric field screening (screening parameter = 0). The azimuthal Euler angle values for each spectra collected at nominal φ are fit. Thicknesses are obtained from the isotropic model and fixed. The polar Euler angle θ is fixed to that obtained from cross-sectional SEM. Fig. 6 shows the anisotropic optical properties over the modeled range for the two as-deposited CdTe films sputtered at $\Phi = 60°$ and 80°. The birefringence, difference in the indices of refraction in extra-ordinary and ordinary direction (n_e-n_o), is greater for $\Phi = 80°$ due to increased shadowing effects at higher angles of incidence. This behavior has also been observed in other GLAD polycrystalline thin films [22,23,52,53].

The post-deposition CdCl$_2$ treatment process is an important step during the fabrication of CdTe solar cells for improving device performance. CdCl$_2$ treatment results in recrystallization, grain growth, grain boundary passivation, and randomizing the crystal orientation [15,16]. CdCl$_2$ treatments are applied to GLAD CdTe films at different oblique angles. Using XRD measurement and Scherrer's equation [54], the crystallite size variations with CdCl$_2$ treatment time are shown in Fig. 7. In the calculation, the diffraction peak centered around 23.7° indexed to C(111) and H(002) is considered. Crystallite size increases after CdCl$_2$ treatment for all samples and increases with increasing treatment time. On average, the crystallite size for all sample increased by ~20% after CdCl$_2$ treatment for the most commonly used 30 min treatment time [3–5] compared to as-deposited samples. Also, surface view SEM
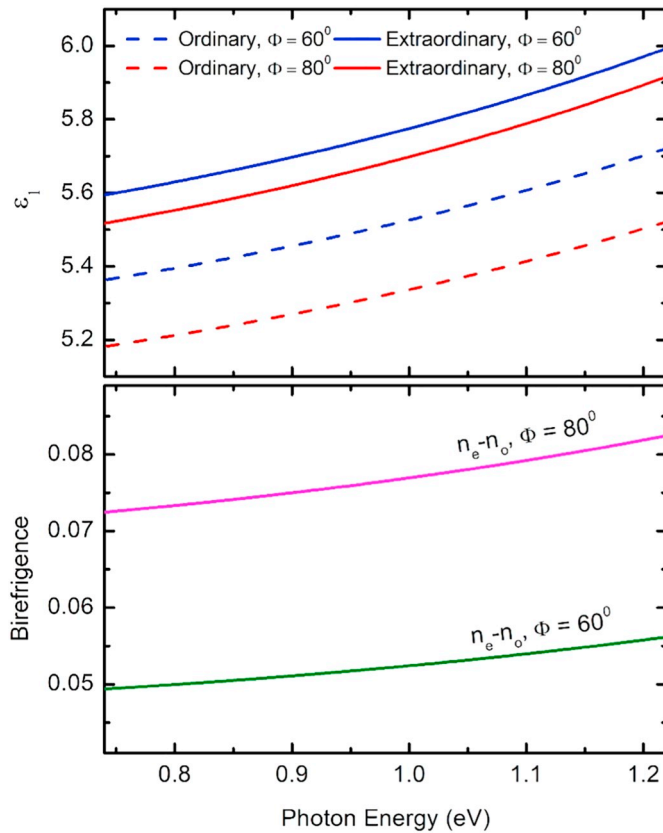
Fig. 6. Anisotropic optical properties parallel (extra-ordinary, *e*) and perpendicular (ordinary, *o*) to the columnar principal axes in (top) ε_1 and (bottom) birefringence, n_e-n_o in the transparent spectral range of CdTe prepared by GLAD at $\Phi = 60°$ and 80°.
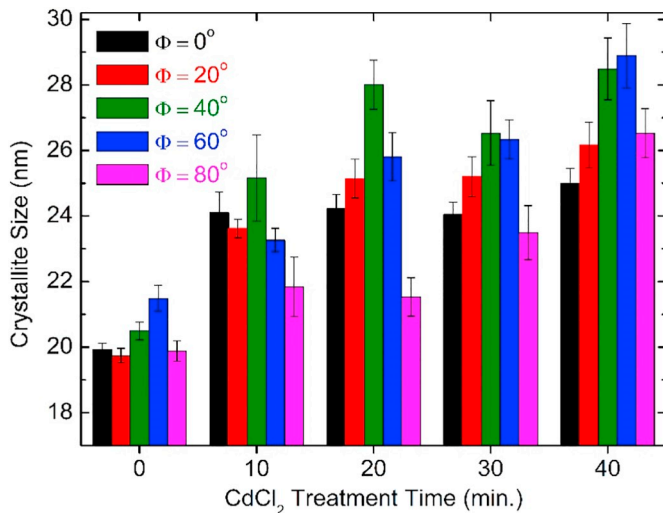
Fig. 7. Crystallite size deduced via the Scherrer equation as a function of CdCl$_2$ treatment time for CdTe deposited at different oblique angles.

have shown enhanced grain size after CdCl$_2$ treatment. Fig. 8 shows an example of surface view SEM images of CdTe film deposited at $\Phi = 0°$ before and after CdCl$_2$ treatment for 30 min. As a result of CdCl$_2$ treatment, the grain size increases from 122 ± 5 nm (before treatment) to 317 ± 7 nm (after treatment).

CdS/CdTe heterojunction solar cells with and without nominally 100 nm thick GLAD wurtzite interfacial layers between the *n*-type CdS window layer and *p*-type zinc blende CdTe absorber have been

fabricated using Cu/Au back contacts (Fig. 2). All CdTe layers are deposited at RT followed by post-deposition CdCl$_2$ treatment. Fig. 9 shows the XRD patterns of $\Phi = 0°$ CdTe absorber layer and $\Phi = 80°$ GLAD CdTe interlayer after CdCl$_2$ treatment along with that of the hexagonal CdS window layer. After CdCl$_2$ treatment, $\Phi = 80°$ GLAD CdTe interlayer exhibits diffraction peaks corresponding to both cubic and hexagonal crystal structures. As some hexagonal phase CdTe crystallites exist after the CdCl$_2$ process, better lattice matching with the underlying CdS can occur. For the absorber layer deposited at $\Phi = 0°$ after CdCl$_2$ treatment, only C(111), C(200), C(220), C(311), C(400), and C(331) index diffraction peaks associated with cubic CdTe are observed. Although the peak position of C(111) and H(002), C(220) and H(110), and C(311) and H(112) are close, the absence of additional hexagonal peaks indicates that the CdTe absorber layer deposited at $\Phi = 0°$ has cubic zinc blende crystal structure after CdCl$_2$ treatment. Also, after CdCl$_2$ treatment, the presence of Cd$_x$TeO$_y$ peaks shows the oxidation of the surface, as expected for these processing conditions.

The Scherrer equation has been used to determine the crystallite size associated with each diffraction peak in as-deposited and CdCl$_2$ treated (30 min) samples prepared at different Φ. Crystallite size associated with H(102) crystallites increases slightly for $\Phi = 40°$ and 60° and remains approximately the same for $\Phi = 80°$ after CdCl$_2$ treatment. The crystallite size associated with the H(103) peak increases for $\Phi = 80°$, is approximately the same for $\Phi = 60°$, and slightly decreases for $\Phi = 40°$. Crystallite size associated with the most dominate crystallite orientations increase with CdCl$_2$ treatment. Cubic phase crystallite orientations become more random after CdCl$_2$ treatment as observed by the appearance of C(200) planes in addition to the C(220), C(111), and C(311) planes prior to treatment. Individual hexagonal phase crystallite orientations become either more or less pronounced after CdCl$_2$ treatment depending upon the initial crystallite orientations present in the samples. These observations imply that the introduction of the thin GLAD CdTe interlayer between the hexagonal CdS and cubic CdTe absorber layer is improving lattice matching on both sides of the junction via alignment of crystal planes. The presence of the interlayer is expected to result in reductions in strain energy, density of unpassivated bonds, or both which is expected to reduce the defect density at the interface.

Fig. 10(a) shows *J-V* characteristics of the highest performing CdS/CdTe solar cells with and without the GLAD CdTe interlayer in the solar cell structure. The open circuit voltage (V_{OC}), short circuit current density (J_{SC}), power conversion efficiency (*PCE*), and fill factor (*FF*) corresponding to devices plotted in Fig. 10 are shown in Table 3. The best device without the GLAD CdTe interlayer has a *PCE* = 10.1% with V_{OC} = 0.728 V, J_{SC} = 23.2 mA/cm^2, and *FF* = 59.4%. After incorporating structurally engineered GLAD CdTe between the *n*-type CdS window layer and normally sputtered *p*-type CdTe absorber, the best device has *PCE* = 11.0% with V_{OC} = 0.774 V, J_{SC} = 23.0 mA/cm^2, and *FF* = 61.9%. Using the GLAD CdTe interlayer, *PCE* increased by 9% relative and 0.9% absolute, and this enhancement in device performance is attributed to an increase in V_{OC} by 6% and FF by 4%. Device performance parameters of all CdS/CdTe heterojunction solar cells with and without GLAD CdTe interlayers are shown in Fig. 11. Out of 256 dot cells, some of the cells show substantially lower performance and hence only the 200 highest performing dot cells are included in the statistical average calculation and one standard deviation variation for both sets of solar cells given in Table 3. The average V_{OC}, J_{SC}, *FF*, and *PCE* of devices with GLAD CdTe interlayers are higher compared to devices without GLAD interlayers. On average, *PCE* is higher for devices with the GLAD interlayer with the largest gain attributed to improved V_{OC}. Fig. 10(b) shows similar EQE spectra over the 300–1000 nm wavelength range for the same highest efficiency devices indicating that the presence of the interlayer does not reduce the spectroscopic optical performance of these solar cells.

Solar cell diode parameters are obtained by fitting experimental *J-V* to the diode equation [55,56]:
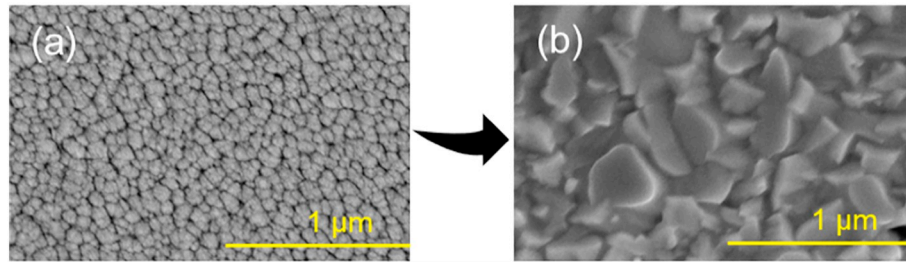
Fig. 8. Surface SEM images of CdTe film deposited at $\Phi = 0°$ (a) before and (b) after CdCl$_2$ treatment for 30 min.
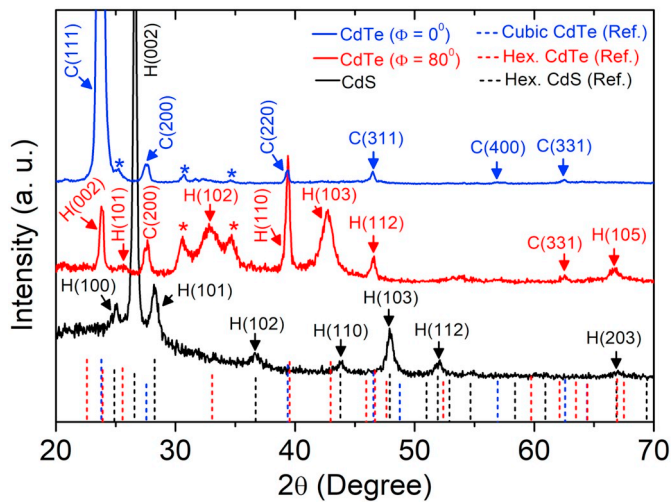
Fig. 9. XRD patterns of CdS (black), CdCl$_2$ treated CdTe ($\Phi = 0°$) (blue), and CdCl$_2$ treated CdTe ($\Phi = 80°$) (red). Peaks associated with Cd$_x$TeO$_y$ are also indicated (*). The vertical lines represent the reference diffraction peak positions for hexagonal CdS (PDF#97-015-4186), cubic CdTe (PDF#97-010-8238), and hexagonal CdTe (PDF#97-015-0941) crystal structures obtained from MDI JADE software. (For interpretation of the references to colour in this figure legend, the reader is referred to the Web version of this article.)

$$J = J_0 \exp\left[\frac{q}{nk_BT}(V - R_SJ)\right] + G_{SH}V - J_L \qquad (1)$$

Here q is the electronic charge, n is the diode ideality factor, k_B is Boltzmann's constant, T is temperature, J_0 is the reverse saturation current, R_S is the series resistance, G_{SH} is the shunt conductance, and J_L is the current density at AM1.5G light illumination. Ideality factors are

calculated by plotting the derivative dV/dJ from the exponential diode equation as a function of $1/J$ when the devices are not illuminated, with results for the highest efficiency devices with and without the GLAD interlayer shown in Fig. 12(a). The slope and intercept of the linear fit give R_S and n, respectively. The calculation results in similar series resistances of 2.4 and 2.1 Ω cm^2 for the devices with and without the GLAD CdTe interlayers and substantially different ideality factors of 2.3 and 3.0, respectively. Similarly, the plot between ln[J] and V-R_SJ using R_s, allows for extraction of n and J_0 for the highest efficiency devices with and without the GLAD interlayer as shown in Fig. 12(b). These values of n are 2.0 and 2.5, and the values of J_0 are 2×10^{-6} mA/cm^2 and 7×10^{-5} mA/cm^2, respectively, for the devices with and without GLAD CdTe interlayers. The values of n and J_0 for these CdTe devices are consistent with values reported in literature for similar devices [55–57]. Overall, lower values of J_0 and n with comparable R_s for the device with the GLAD CdTe interlayer indicates improvement in the diode performance parameters. The lower values of n and J_0 for the highest efficiency cell with the GLAD interlayer compared to the highest efficiency device without the interlayer indicates lower recombination of charge carriers due to the formation of an improved electronic quality interface [57]. The resulting improvement in diode parameters leads to increases in V_{OC}, FF, and overall solar cell performance as observed for devices incorporating the GLAD CdTe interlayer.

The better performance of device with the GLAD interlayer can be attributed to an improved n/p interface due to less lattice mismatch between wurtzite CdS and hexagonal wurtzite phase crystallites in the GLAD CdTe interlayer, as both share the same crystal structure and more similar lattice constants when compared to zinc blende CdTe. As a result, wurtzite CdTe incorporated in these devices makes higher electronic quality, less defective interfaces with the underlying wurtzite CdS and over-deposited zinc blende CdTe [58,59]. All these results indicate that the idea of incorporating a thin GLAD CdTe interlayer between CdS and zinc blende CdTe serves as a means of interfacial
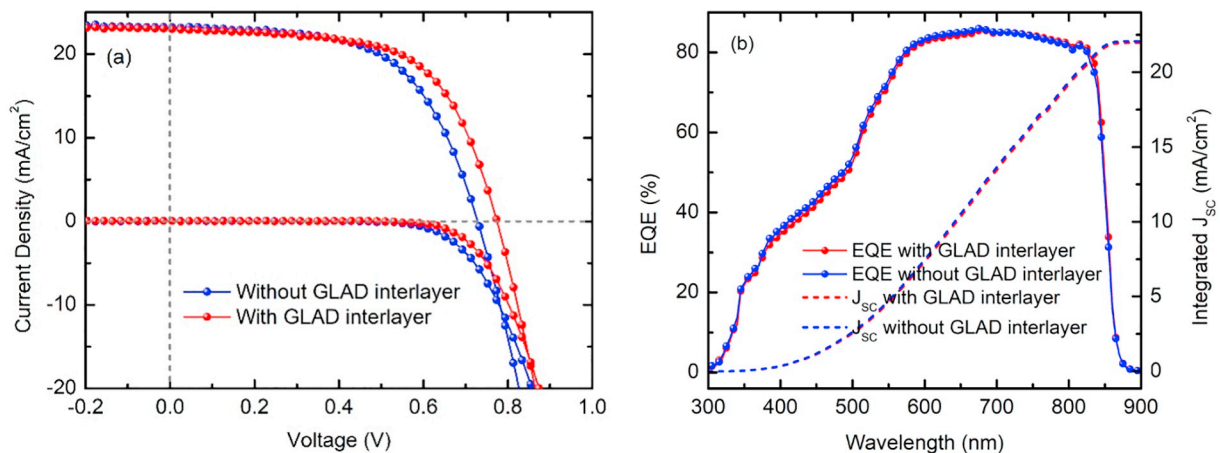
Fig. 10. Device performance for the highest efficiency solar cells with and without a 100 nm GLAD CdTe interlayer: (a) light and dark current-voltage (J-V) and (b) external quantum efficiency (EQE) for CdS/CdTe heterojunction solar cells with (red) and without (blue) introduction of the GLAD interlayer. (For interpretation of the references to colour in this figure legend, the reader is referred to the Web version of this article.)

Table 3

Comparison of device performance parameters of highest efficiency CdS/CdTe solar cells with and without a 100 nm thick GLAD CdTe interlayer. Average performance parameters with one standard deviation (1-σ) variation for the best 200 (out of 256) small area devices for each configuration are also given.

Solar cell parameter		V_{OC} (V)	J_{SC} (mA/cm^2)	PCE (%)	FF (%)
Without interlayer	Best cell	0.728	23.2	10.1	59.4
	Average of 200 cells	0.710 ± 0.032	20.0 ± 1.8	7.72 ± 1.04	54.1 ± 3.1
With interlayer	Best cell	0.774	23.0	11.0	61.9
	Average of 200 cells	0.730 ± 0.030	20.4 ± 1.3	8.10 ± 1.25	54.2 ± 3.7

tailoring at the heterojunction for improving PV device performance. This concept will be extended for devices incorporating more optimized CdTe after deposition of the interlayer, as opposed to RT normal incidence deposited CdTe.

4. Conclusions

GLAD magnetron sputtered CdTe shows variation in optical properties, density, and microstructure with incident oblique angle. Crystal phase structure transitions from mixed-phase cubic zinc blende and hexagonal wurtzite crystal structures to the hexagonal phase with increasing oblique angle. As-deposited GLAD CdTe films prepared at higher oblique angles show sensitivity to in-plane optical anisotropy from the projection of the tilted columnar axes and as identified from analysis of Mueller matrix spectra. CdCl$_2$ treated CdTe shows enhanced

crystallite size compared to as-deposited samples with crystallite size increasing with treatment time. PV devices incorporating GLAD CdTe interlayer show 0.9% absolute higher efficiency compared to devices without the interlayer. The higher efficiency of the device with GLAD CdTe interlayer is because of an improved *n/p* interface due to improved structural compatibility between CdS and wurtzite phase crystallites in the GLAD CdTe interlayer.

Disclaimer text

The views and conclusions contained herein are those of the authors and should not be interpreted as necessarily representing the official policies or endorsements, either expressed or implied, of Air Force Research Laboratory or the U.S. Government.
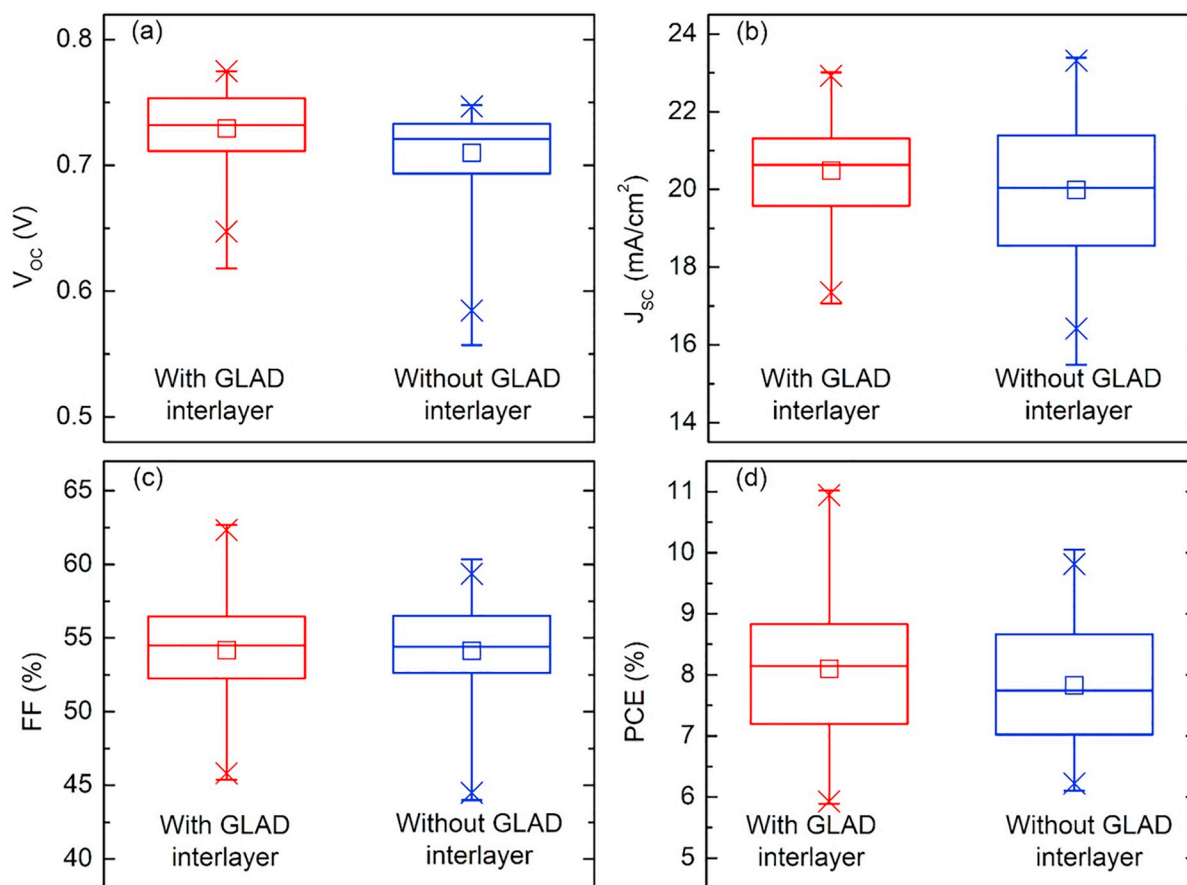
Fig. 11. (a) Open circuit voltage (V_{OC}), (b) short circuit current density (J_{SC}), (c) fill factor (*FF*), and (d) power conversion efficiency (*PCE*) parameter ranges for all CdTe PV devices with and without GLAD CdTe interlayers.
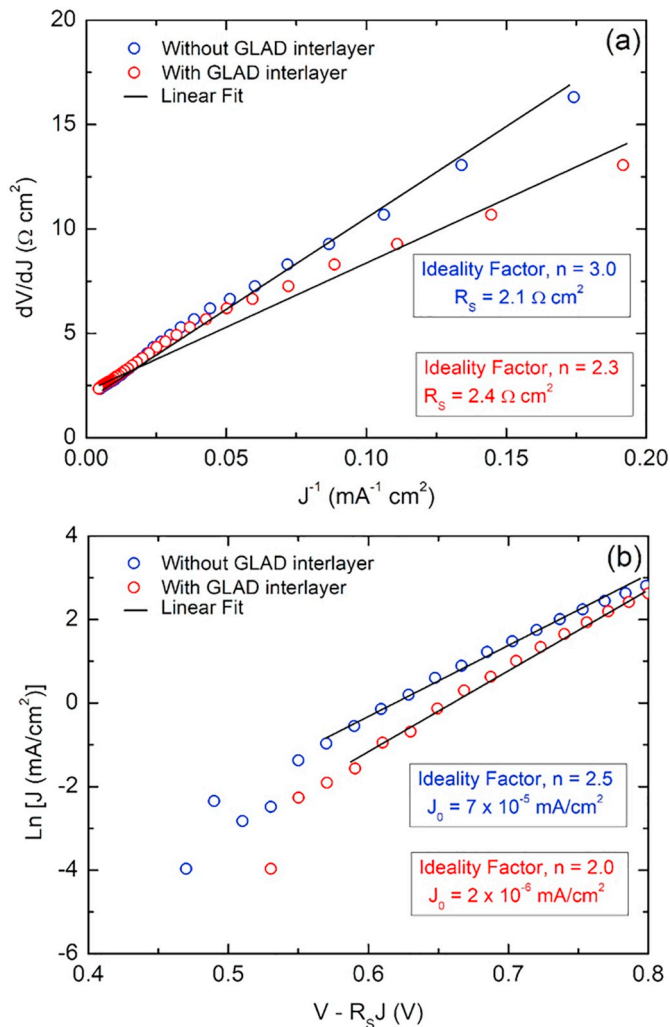
Fig. 12. Analysis of dark current density versus voltage characteristics for the best performing CdS/CdTe heterojunction solar cells with and without GLAD CdTe interlayers: (a) dV/dJ versus $1/J$ plot for calculation of n and R_S and (b) semi-log scale plot for the calculation of J_0 and n.

Declaration of competing interest

The authors declare that they have no known competing financial interests or personal relationships that could have appeared to influence the work reported in this paper.

Acknowledgement

References

[1] A. Gupta, A.D. Compaan, All-sputtered 14% CdS/CdTe thin-film solar cell with ZnO: Al transparent conducting oxide, Appl. Phys. Lett 85 (2004) 684–686.
[2] A. Gupta, V. Parikh, A.D. Compaan, High efficiency ultra-thin sputtered CdTe solar cells, Sol. Energy Mater. Sol. Cells 90 (2006) 2263–2271.
[3] P. Koirala, J. Li, H.P. Yoon, P. Aryal, S. Marsillac, A.A. Rockett, N.J. Podraza, R.W. Collins, Through-the-glass spectroscopic ellipsometry for analysis of CdTe thin-film solar cells in the superstrate configuration, Prog. Photovolt. Res. Appl. 24 (2016) 1055–1067.
[4] M. Tuteja, P. Koirala, S. MacLaren, R. Collins, A. Rockett, Direct observation of

[5] electrical properties of grain boundaries in sputter-deposited CdTe using scan-probe microwave reflectivity based capacitance measurements, Appl. Phys. Lett. 107 (2015) 142106.
[5] N.R. Paudel, K.A. Wieland, A.D. Compaan, Ultrathin CdS/CdTe solar cells by sputtering, Sol. Energy Mater. Sol. Cells 105 (2012) 109–112.
[6] J.L. Boone, T.P. Van Doren, A.K. Berry, Deposition of CdTe by spray pyrolysis, Thin Solid Films 87 (1982) 259–264.
[7] A.E. Rakhshani, Electrodeposited CdTe-optical properties, J. Appl. Phys. 81 (1997) 12.
[8] X. Wu, High-efficiency polycrystalline CdTe thin-film solar cells, Sol. Energy 77 (2004) 803–814.
[9] J. Britt, C. Ferekides, Thin-film CdS/CdTe solar cell with 15.8% efficiency, Appl. Phys. Lett. 62 (1993) 2851–2852.
[10] M.A. Green, Y. Hishikawa, E.D. Dunlop, D.H. Levi, J. Hohl-Ebinger, M. Yoshita, A.W.Y. Ho-Baillie, Solar cell efficiency tables (Version 53), Prog. Photovolt. Res. Appl. 27 (2019) 3–12.
[11] Research Progress Report, Institute of Electrical Engineering, Chinese Academy of Science, (2014).
[12] K.D. Dobson, I. Visoly-Fisher, G. Hodes, D. Cahen, Stability of CdTe/CdS thin-film solar cells, Sol. Energy Mater. Sol. Cells 62 (2000) 295–325.
[13] C. Li, Y. Wu, J. Poplawsky, T.J. Pennycook, N. Paudel, W. Yin, S.J. Haigh, M.P. Oxley, A.R. Lupini, M. Al-Jassim, S.J. Pennycook, Y. Yan, "Grain-boundary-enhanced carrier collection in CdTe solar cells, Phys. Rev. Lett. 112 (2014) 156103.
[14] I. Visoly-Fisher, S.R. Cohen, A. Ruzin, D. Cahen, "How polycrystalline devices can outperform single-crystal ones: thin film CdTe/CdS solar cells, Adv. Mater. 16 (2004) 879–883.
[15] N.G. Dhere, R.G. Dhere, Thin-film photovoltaics, J. Vac. Sci. Technol. A 23 (2005) 1208–1214.
[16] B. McCandless, J. Sites, A. Luque, S. Hegedus (Eds.), Handbook of Photovoltaic Science and Engineering, Wiley, Chichester, England, 2003.
[17] M.H. Ehsani, H. RezagholipourDizaji, S. Azizi, S.F. Ghavami Mirmahalle, F. Hosseini Siyanaki, Optical and structural properties of cadmium telluride films grown by glancing angle deposition, Phys. Scr. 88 (2013) 025602.
[18] D. Adhikari, P. Koirala, M.M. Junda, R.W. Collins, N.J. Podraza, Glancing angle deposited CdTe: optical properties and structure, IEEE 7th World Conference on Photovoltaic Energy Conversion (WCPEC) (A Joint Conference of 45th IEEE PVSC, 28th PVSEC & 34th EU PVSEC), 2018 DOI: 10.1109/PVSC.2018.8547890.
[19] J. Lee, P.I. Rovira, I. An, R.W. Collins, Rotating-compensator multichannel ellipsometry: applications for real time Stokes vector spectroscopy of thin film growth, Rev. Sci. Instrum. 69 (1998) 1800–1810.
[20] B. Johs, J.A. Woollam, C.M. Herzinger, J. Hilfiker, R. Synowicki, C.L. Bungay, Overview of variable angle spectroscopic ellipsometry (VASE), Part II: advanced applications, Proc. SPIE 72 (1999) 29–58.
[21] C. Chen, I. An, G.M. Ferreira, N.J. Podraza, J.A. Zapien, R.W. Collins, Multichannel Mueller matrix ellipsometer based on the dual rotating compensator principle, Thin Solid Films 14 (2004) 455–456.
[22] N.J. Podraza, Chi Chen, J.M. Flores, D. Sainju, llsin An, G.M. Ferreira, C.R. Wronski, M.W. Horn, R. Messier, R.W. Collins, Optical properties of transparent conducting oxide sculptured thin films silicon photovoltaics, Proc. IEEE 31st Photovoltaics Specialists Conf, 2005, pp. 1428–1431 DOI: 10.1109/PVSC.2005.1488409.
[23] N.J. Podraza, Chi Chen, D. Sainju, O. Ezekoye, M.W. Horn, C.R. Wronski, R.W. Collins, "Transparent conducting oxide sculptured thin films for photovoltaic applications, Proc. Mat. Res. Soc. Symp. 865 (F7.1) (2005) 1–6.
[24] J.M. Nieuwenhuizen, H.B. Haanstra, Microfractography of thin films, Philips Tech. Rev. 27 (1966) 87–91.
[25] A.G. Dirks, H.J. Leamy, Columnar microstructure in vapor-deposited thin films, Thin Solid Films 47 (1977) 219–233.
[26] R.N. Tait, T. Smy, M.J. Brett, Modelling and characterization of columnar growth in evaporated films, Thin Solid Films 226 (1993) 196–201.
[27] S. Lichter, J. Chen, Model for columnar microstructure of thin solid films, Phys. Rev. Lett. 56 (1986) 1396–1399.
[28] R. Álvarez, L. González-García, P. Romero-Gómez, V. Rico, J. Cotrino, A.R. González-Elipe, A. Palmero, Theoretical and experimental characterization of TiO2 thin films deposited at oblique angles, J. Phys. D Appl. Phys. 44 (2011) 385302.
[29] P. Morrow, F. Tang, T. Karabacak, P.I. Wang, D.X. Ye, G.C. Wang, T.M. Lu, Texture of Ru columns grown by oblique angle sputter deposition, J. Vac. Sci. Technol. A 24 (2006) 235–245.
[30] M.M. Hawkeye, M.J. Brett, Glancing angle deposition: fabrication, properties, and applications of micro- and nanostructured thin films, J. Vac. Sci. Technol. A 25 (2007) 1317–1335.
[31] E. Alfonso, J. Olaya, G. Cubillos, Thin film growth through sputtering technique and its applications, in: M. Andreeta (Ed.), Crystallization-Science and Technology, Intech, Croatia, 2012, pp. 397–432.
[32] P. Gu, X. Zhu, H. Wu, D. Yang, Regulation of substrate-target distance on the microstructural, optical, and electrical properties of CdTe films by magnetron sputtering, Materials 11 (2018) 2496.
[33] R. Kulkarni, S. Rondiya, A. Pawbake, R. Waykar, A. Jadhavar, V. Jadkar, A. Bhorde, A. Date, H. Pathan, S. Jadkar, Structural and optical properties of CdTe thin films deposited using RF magnetron sputtering, Energy Procedia 110 (2017) 188–195.
[34] F. Hosseinpanahi, D. Raoufi, K. Ranjbarghanei, B. Karimi, R. Babaei, E. Hasani, Fractal features of CdTe thin films grown by RF magnetron sputtering, Appl. Surf. Sci. 357 (2015) 1843–1848.
[35] S.A. Alterovitz, B. Johs, Multiple minima in the ellipsometric error function, Thin Solid Films 124 (1998) 313–314.
[36] D.E. Aspnes, M. Balkanski (Ed.), Handbook of Semiconductors, vol. 2, North-

Holland, Amsterdam, The Netherlands, 1980.

[37] R.W. Collins, A.S. Ferlauto, H.G. Tompkins, E.A. Irene (Eds.), Handbook of Ellipsometry, William Andrew publishing, Norwich, 2005.

[38] G.E. Jellison Jr., F.A. Modine, Parameterization of the optical functions of amorphous materials in the interband region, Appl. Phys. Lett. 69 (1996) 371–373.

[39] G.E. Jellison, F.A. Modine, Erratum: 'Parameterization of the optical functions of amorphous materials in the interband region', Appl. Phys. Lett. *69* (1996) 371–373. *Appl. Phys. Lett.,* 69 (1996) 2137.

[40] H. Fujiwara, J. Koh, P. Rovira, R. Collins, Assessment of effective-medium theories in the analysis of nucleation and microscopic surface roughness evolution for semiconductor thin films, Phys. Rev. B 61 (2000) 10832–10844.

[41] J.A. Zapien, J. Chen, J. Li, J. Inks, N.S. Podraza, C. Chen, J. Drayton, A. Vasko, A. Gupta, S.L. Wang, R.W. Collins, A.D. Compaan, Real time spectroscopic ellipsometry of thin film CdTe deposition by magnetron sputtering for photovoltaic applications, IEEE 31st Photovoltaics Specialists Conf. 2005, pp. 461–464 DOI: 10.1109/PVSC.2005.1488169.

[42] J. Li, J. Chen, M.N. Sestak, C. Thornberry, R.W. Collins, Spectroscopic ellipsometry studies of thin film CdTe and CdS: from dielectric functions to solar cell structures, Proc. IEEE 34th Photovoltaics Specialists Conf. 2009, pp. 001982–001987 DOI: 10.1109/PVSC.2009.5411520.

[43] J. Li, N.J. Podraza, R.W. Collins, Real time spectroscopic ellipsometry of sputtered CdTe, CdS, and CdTe$_{1-X}$ S$_X$ thin films for photovoltaic applications, Phys. Status Solidi A 205 (2008) 901–904.

[44] W.G. Oldham, Numerical techniques for the analysis of lossy films, Surf. Sci. 16 (1969) 97–103.

[45] J. Li, J. Chen, R.W. Collins, Optical transition energies as a probe of stress in polycrystalline CdTe thin films, Appl. Phys. Lett. 99 (2011) 061905.

[46] B. Johs, C.M. Herzinger, J.H. Dinan, A. Cornfeld, J.D. Benson, Development of a parametric optical constant model for Hg$_{1-x}$Cd$_x$Te for control of composition by spectroscopic ellipsometry during MBE growth, Thin Solid Films 137 (1998) 313–314.

[47] C.C. Kim, M. Daraselia, J.W. Garland, S. Sivanathan, Temperature dependence of the optical properties of CdTe, Phys. Rev. *B* 56 (1997) 4786–4797.

[48] S. Jiménez-Sandoval, M. Meléndez-Lira, I. Hernández-Calderón, Crystal structure and energy gap of CdTe thin films grown by radio frequency sputtering, J. Appl. Phys. 72 (1992) 4197–4202.

[49] S.M. Hosseini, Optical properties of cadmium telluride in zinc-blende and wurzite structure, Physica *B* 403 (2008) 1907–1915.

[50] D. Adhikari, M.M. Junda, P. Uprety, K. Ghimire, I. Subedi, N.J. Podraza, Near infrared to ultraviolet anisotropic optical properties of single crystal SrLaAlO$_4$ from spectroscopic ellipsometry, Phys. Status Solidi B 253 (2016) 2066–2072.

[51] D.E. Aspens, Optical properties of thin films, Thin Solid Films 89 (1982) 249–262.

[52] S. Wang, X. Fu, G. Xia, J. Wang, J. Shao, Z. Fan, Structure and optical properties of ZnS thin films grown by glancing angle deposition, Appl. Surf. Sci. 252 (2006) 8734–8737.

[53] R.B. Tokas, S. Jena, S.M. Haque, K.D. Rao, S. Thakur, N.K. Sahoo, Spectroscopic ellipsometry investigations of optical anisotropy in obliquely deposited Hafnia thin films, AIP Conf. Proc. 1731 (2016) 060007, https://doi.org/10.1063/1.4947813.

[54] P. Scherrer, Nachrichten von der gesellschaft der wissenschaftenzugöttingen, Mathematisch-PhysikalischeKlasse 2 (1918) 98.

[55] S.S. Hegedus, W.N. Shafarman, Thin-film solar cells: device measurements and analysis, Prog. Photovolt. Res. Appl. 12 (2004) 155–175.

[56] K.P. Bhandari, X. Tan, P. Zereshki, F.K. Alfadhili, A.B. Phillips, P. Koirala, M.J. Heben, R.W. Collins, R.J. Ellingson, Thin film iron pyrite deposited by hybrid sputtering/co-evaporation as a hole transport layer for sputtered CdS/CdTe solar cells, Sol. Energy Mater. Sol. Cells 163 (2017) 277–284.

[57] S. Marsillac, V.Y. Parikh, A.D. Compaan, Ultra-thin bifacial CdTe solar cell, Sol. Energy Mater. Sol. Cells 91 (2007) 1398–1404.

[58] H.C. Chou, A. Rohatgi, N.M. Jokerst, S. Kamra, S.R. Stock, S.L. Lowrie, R.K. Ahrenkiel, D.H. Levi, Approach toward high efficiency CdTe/CdS heterojunction solar cells, Mater. Chem. Phys. 43 (1996) 178–182.

[59] X. Wu, R.G. Dhere, Y. Yan, M.J. Romero, Y. Zhang, J. Zhou, C. DeHart, A. Duda, C. Perkins, B. To, High-efficiency polycrystalline CdTe thin-film solar cells with an oxygenated amorphous CdS (a-CdS: O) window layer, Proc. IEEE 29th Photovoltaics Specialists Conf. 2002, pp. 1–4 DOI: 10.1109/PVSC.2002.1190619.